International Journal of Fatigue 155 (2022) 106577

Contents lists available at ScienceDirect

International Journal of Fatigue

journal homepage: www.elsevier.com/locate/ijfatigue

High-cycle and very-high-cycle fatigue lifetime prediction of additively manufactured AlSi10Mg via crystal plasticity finite element method

Jiamei Zhang [a], Jianghua Li [a], Shengchuan Wu [b], Wenjie Zhang [c], Jingyu Sun [a,*], Guian Qian [a,*]

[a] State Key Laboratory of Nonlinear Mechanics (LNM), Institute of Mechanics, Chinese Academy of Sciences, Beijing 100190, China
[b] State Key Laboratory of Traction Power, Southwest Jiaotong University, Chengdu 610031, China
[c] Sino-French Institute of Nuclear Engineering and Technology, Sun Yat-Sen University, Zhuhai 519082, Guangdong, China

ARTICLE INFO

Keywords:
Crystal plasticity
Additive manufacturing
Very-high-cycle fatigue
AlSi10Mg alloy
Defects

ABSTRACT

The effects of defects and building directions in additive manufactured AlSi10Mg on its high-cycle fatigue and very-high-cycle fatigue performance are studied based on crystal plasticity finite element (CPFE). Among the three models provided in this work, the results of model 2 (N_{p2}) are in good agreement with the experimental ones. It is found the fatigue life of the sample with defects are much lower than that without defects. 0° specimens have a better fatigue performance than 90° ones. This work is beneficial in determining the fatigue lifetime and helps to improve the fatigue behavior of AlSi10Mg.

1. Introduction

Aluminium (Al) and its alloys are characterized by their light weight, high strength, corrosion resistance, and good weldability, making them suitable for a range of applications in industries such as automotive, aerospace, machinery and tooling, defence, and construction [1,2]. Engineering components comprising Al alloys are traditionally fabricated by processes such as casting, forging, extrusion, and powder metallurgy [3]. In recent years, with the development of additive manufacturing (AM) technologies, aluminium–silicon-based alloys (Al-Si), specifically AlSi10Mg, owing to fabricability, have been fabricated by the selective laser melting (SLM) process, which is an AM technology [4,5].

SLM technologies are more environmentally friendly compared to traditional manufacturing processes, due to their rapid manufacturing processes, high material utilization and potential for a nearly 50% reduction in weight. However, the inherent defects resulting from the SLM process are inevitable. Thus SLM technology, despite its enormous potential, introduces uncertainty in the mechanical performance of the parts, which prohibits the use of these materials in safety–critical components [6,7]. Particularly, the defects resulting from SLM processes can induce crack initiation and thus significantly reduce the fatigue properties of the samples [8-11]. Thus, many researchers have considered the effects of surface roughness, AM process parameters, heat treatment processes and building directions on fatigue performance[12-15].

Previous studies have indicated that the size, location, and shape of defects are essentially responsible for the behavior of high-cycle fatigue (HCF) data of AM metals [16,17]. Generally, larger defects on or beneath the surface are more likely to drive fatigue failure as a result of concentrating high local stress. In such case, the fatigue strength is mainly governed by the largest defect within the surface volume [13,18], while excluding the collaborative effect of residual stress and surface quality [19]. And many factors can affect the defect population and its size: in particular, the platform heating [20], the scanning strategy and the process [21,22] and, above all, the part orientation with respect to the building direction [23]. While low-temperature heat treatments do not affect defect size [24].

Besides, AM building directions had an obvious impact on the fatigue crack propagation resistance and fatigue limits of the SLM-ed AlSi10Mg samples [9], and the fatigue limits of the 45° and 90° samples were lower than that of the 0° sample. This is because the 45° and 90° samples have a higher density of defects distributed on the crack propagation paths, which is parallel to the direction of the SLM deposition layers (or perpendicular to the building direction) [25]. Additionally, for the 0° samples the maximum defect area was far less than those of the 45° and 90° samples. Due to the highly directional columnar grain structures, the as-built materials also exhibit obvious anisotropic properties which can cause the premature failure of AM components during service [26].

Since the beginning of the 20th century, a lot of researchers proposed

* Corresponding authors.
E-mail addresses: sunjingyu@imech.ac.cn (J. Sun), qianguian@imech.ac.cn (G. Qian).

https://doi.org/10.1016/j.ijfatigue.2021.106577
Received 7 June 2021; Received in revised form 13 September 2021; Accepted 1 October 2021
Available online 5 October 2021
0142-1123/

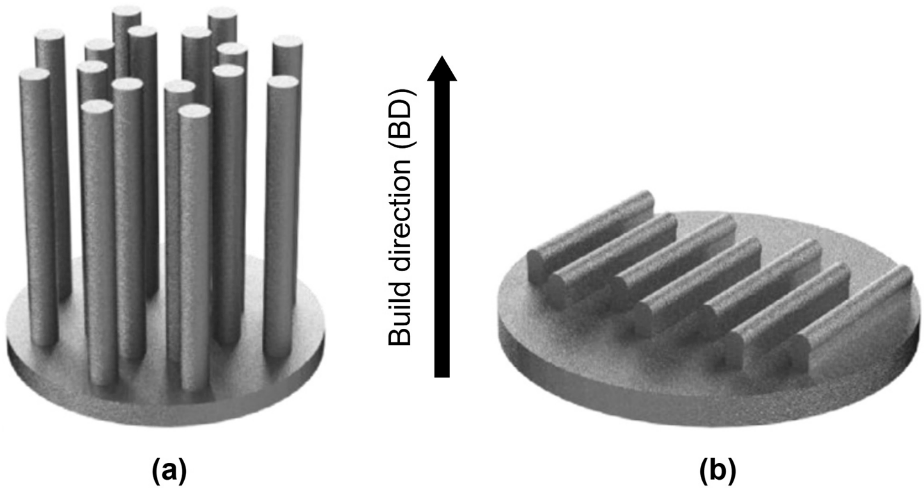

Fig. 1. The fatigue samples of SLM-ed AlSi10Mg alloy: (a) 90° BD sample; (b) 0° BD sample [11].

numerous criteria to predict fatigue life under different loading conditions. Basquin [27] offered a phenomenological model in which the stress amplitude and fatigue life are related via a power-law relationship. Later, Coffin [28] and Manson [29] emphasized the importance of plastic strain in predicting the fatigue life at low-cycle fatigue (LCF) regime. Then, a model connecting the plastic energy with fatigue life was proposed by Morrow [30], following whose footsteps a series of researchers employed energy-based approaches in fatigue life predicting [31-33].

Recently, with the increasing demands of safety requirements, more and more engineering components are designed to endure a fatigue life of more than 10^7 cycles (known as the very-high-cycle fatigue, VHCF), even up to 10^8 and 10^9 cycles [34]. As for LCF, only a few number of loading cycles is consumed to initiate cracks. However, in the HCF and VHCF regimes, more than 80–90% of fatigue life would be consumed in the crack initiation stage [35], which differs completely from that in LCF regimes. In addition, the unique feature of crack initiation for VHCF of high-strength alloys is that fatigue cracks initiate from the interior of material or specimen, which is the essential point that differs from LCF and HCF cases. Crack initiation of VHCF for metallic materials possesses a unique feature of fish-eye (FiE) which contains a fine-granular-area (FGA). It is regarded that FGA together with FiE is the characteristic region of crack initiation for VHCF, and the value of stress intensity factor range for this region keeps constant for a given material [36].

In the past two decades, several researchers proposed some models to explain the formation mechanism of crack initiation region in VHCF regimes [37-39]. Zhao et al. [40] analyzed the relationship between the plastic zone size ahead of FGA crack tip and the dimension of related microstructure. Murakami et al. [41] provided the formulas of the maximum value of stress intensity factor (K_{Imax}) for the problems of a crack originating from surface defect or from interior defect. Recently, based on the revealed microscopic nature of crack initiation region of VHCF, Hong et al. [42] proposed a model of Numerous Cyclic Pressing (NCP) to explain the formation mechanism of FGA.

Statistical extremes of fatigue lifetime distribution have been primarily based on large number of experimental data [43]. The experimental results have indicated a scatter in HCF and VHCF lifetime, which is because of the variability in microstructures and defect distribution [44]. However, both the data acquisition and microstructure reconstruction in experiments are extremely slow and redundant. One best way to improve the prediction efficiency of fatigue performance for SLM-ed AlSi10Mg is to use the advanced computation techniques, crystal plasticity finite element (CPFE) frameworks [45,46]. CPFE method has enabled us to implement complex algorithms to model the non-linear material response on the *meso*-scale behavior of crystalline metallic systems with a better approximation [47,48]. Researchers have used CPFE simulation to offer microstructure-sensitive fatigue life prediction frameworks. For example, inspired by the critical plane approach proposed by Fatemi and Socie [49], McDowell and co-workers [50-54] suggested a fatigue indicative parameter accounting for microstructural heterogeneities with the CPFE simulations.

In this paper, the HCF and VHCF behaviors of SLM-ed AlSi10Mg alloy were studied based on CPFE simulations. The goal is to understand the effect and mechanism of build orientation and defects on the fatigue properties of the SLM-ed AlSi10Mg alloy. This paper is structured as follows. The material processing information is detailed in Section 2. The theoretical framework of crystal plasticity is described in Section 3. Section 4 offers the modeling process of CPFE simulations. In Section 5, we provide three fatigue indicator parameter (FIP) models to assess the HCF and VHCF properties of SLM-ed AlSi10Mg alloy. In Section 6, the results are discussed. Finally, concluding remarks are presented.

2. Materials and SLM-ed samples

In this study, the AlSi10Mg samples were fabricated in 0° and 90° building directions (BD), as shown in Fig. 1. The main chemical compositions of the alloy are listed in Table 1. The process parameters of SLM manufacturing are listed in Table 2. The mechanical properties of the AlSi10Mg samples (elastic modulus E, 0.2% offset yield strength $\sigma_{0.2}$, ultimate tensile strength σ_{b}, elongation after fracture δ) were obtained by the uniaxial tensile tests, and the data are listed in Table 3.

The geometries of the tensile and fatigue test specimens are respectively shown in Fig. 2. The design of the AlSi10Mg tensile test specimens was in accordance to the standard of GB/T228-2002. For each group of specimens, six specimens were tested at a tension rate of 2 mm/min. An ultrasonic fatigue machine with a resonance frequency of 20 kHz was used for the fatigue tests. The experiments were carried out by the displacement control in the range between 2.2 μm and 21.5 μm. The

Table 1
Nominal chemical composition of AlSi10Mg alloy (wt.%) [55].

Al	Si	Mg	Fe	Ti	Cu	Cr	Mn	Ni
Bal.	9.75	0.22	0.092	0.011	<0.01	<0.01	<0.01	<0.01

Table 2
SLM manufacturing parameters of the AlSi10Mg specimens.

Laser power [W]	Scanning speed [mm/s]	Scanning spacing [mm]	Preheating temperature [°C]	Layer thickness [mm]	Printing direction [°]	Laser profile
370	1300	0.19	35	0.05	0, 90	Gaussian

Table 3
Mechanical properties of the SLMed-AlSi10Mg alloy.

Sample	*E*, GPa	$\sigma_{0.2}$, MPa	σ_b, MPa	*δ*, %
90°	65.5 ± 3	234.3 ± 4	437 ± 6	4.7 ± 0.5
0°	62 ± 3	280 ± 4	465 ± 6	11.8 ± 0.5

AlSi10Mg specimens under three stress ratios (R = −1, 0, 0.5) were used in the experiment. Ten specimens were tested under each stress ratio. Detailed experimental techniques and results can be found in [55].

Fig. 3 displays the electron backscattering diffraction (EBSD) for the initial microstructures of the SLM-ed samples. In Fig. 3(a), equiaxed grain morphology can be seen in the TD-RD plane which is perpendicular to BD. While Fig. 3(b) exhibits obviously columnar grain morphology in the BD-TD plane which is parallel to BD. Similar phenomena exist both in 0° and 90° specimens, thus only the results of 90° specimens were displayed in this paper. Both in Fig. 3(a) and (b), the pole figure maps on the right reflect that the microstructure of the SLM-ed samples did not show evident texture.

To better model the size and shape of the grains used in this study, we performed a statistical analysis of the columnar grain in the TD-RD plane and BD-TD plane with the EBSD results, as shown in Figs. 4 and 5. Fig. 4 shows the average grain size is 9.61 μm, and Fig. 5 indicates the average aspect ratio of the columnar grain is 4.62. For convenience, in the subsequent simulations, we take the grain size as 10 μm in the plane perpendicular to BD, and the aspect ratio as 5 for the columnar grain.

In this work, the failure modes due to crystallographic features and defects are primarily considered. The role of residual stresses was not considered. In addition, a uniform surface roughness (the maximum height of the profile R_a, the distance between the profile peak line and valley line, was approximately 2.746 μm) was achieved, which is much smaller than the size of the AlSi10Mg powders. Therefore, the effect of sample surface roughness on the fatigue properties of the SLM-ed AlSi10Mg alloy is ignored.

3. Crystal plasticity framework

In the following sections, a CPFE framework accommodating finite deformation effects is used. The governing equations, for single crystals in a continuum framework, will be introduced to provide a background. The kinematics uses a multiplicative decomposition of the deformation gradient. And the phenomenological constitutive relationships incorporating microscopic behaviors in the material will then be given.

3.1. Kinematics

The following kinematic theory is based on the work described in [56,57]. The total deformation gradient **F** obeys a multiplicative decomposition is given in the following equation,

$$\mathbf{F} = \mathbf{F}_e \cdot \mathbf{F}_p \tag{1}$$

where $\mathbf{F}_e$ represents the elastic deformation gradient associated with rigid body rotation and elastic stretching of the crystal lattice, and $\mathbf{F}_p$ is the plastic deformation gradient associated with crystallographic slip.

The velocity gradient in the current state can be calculated using the following equation,

$$\mathbf{L} = \dot{\mathbf{F}} \cdot \mathbf{F}^{-1} = \mathbf{L}_e + \mathbf{L}_p \tag{2}$$

where $\mathbf{L}_e$ is the elastic velocity gradient, and $\mathbf{L}_p$ is the plastic velocity gradient. **L** can be then decomposed into two parts: the symmetric rate of stretching tensor **D** and the antisymmetric spin tensor **Ω**. These two tensors can be decomposed into lattice parts (subscript e) and plastic parts (subscript p) as follows:

$$\mathbf{L} = \mathbf{D} + \mathbf{\Omega} \tag{3}$$

$$\mathbf{D} = \mathbf{D}_e + \mathbf{D}_p \tag{4}$$

$$\mathbf{\Omega} = \mathbf{\Omega}_e + \mathbf{\Omega}_p \tag{5}$$

$\mathbf{L}_e$ and $\mathbf{L}_p$ can be calculated using the following equations,

$$\mathbf{L}_e = \mathbf{D}_e + \mathbf{\Omega}_e = \dot{\mathbf{F}}_e \cdot \mathbf{F}_e^{-1} \tag{6}$$

$$\mathbf{L}_p = \mathbf{D}_p + \mathbf{\Omega}_p = \dot{\mathbf{F}}_p \mathbf{F}_p^{-1} = \sum_{\alpha=1}^{N_s} \dot{\gamma}^{\alpha} \mathbf{s}^{*\alpha} \mathbf{m}^{*\alpha} \tag{7}$$

where N_s is the number of slip systems; $\dot{\gamma}^{\alpha}$ is the slip rate on slip system α; $\mathbf{s}^{*\alpha}$ and $\mathbf{m}^{*\alpha}$ represent the vector along the slip direction and the vector normal to the slip plane of system α, respectively, in the deformed configuration,

$$\mathbf{s}^{*\alpha} = \mathbf{F}_e \cdot \mathbf{s}^{\alpha} \tag{8}$$

$$\mathbf{m}^{*\alpha} = \mathbf{m}^{\alpha} \cdot \mathbf{F}_e^{-1} \tag{9}$$

where $\mathbf{s}^{\alpha}$ and $\mathbf{m}^{\alpha}$ are the unit vectors in the slip direction and normal to the slip plane in the reference configuration, respectively.

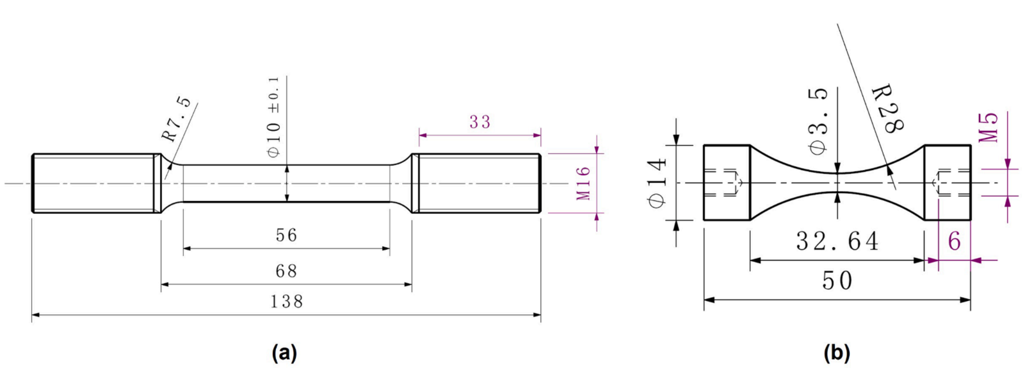

Fig. 2. Geometry of (a) tensile test specimens under monotonic quasi-static loading, and (b) fatigue test specimens under ultrasonic axial cycling (dimensions in mm) [55].

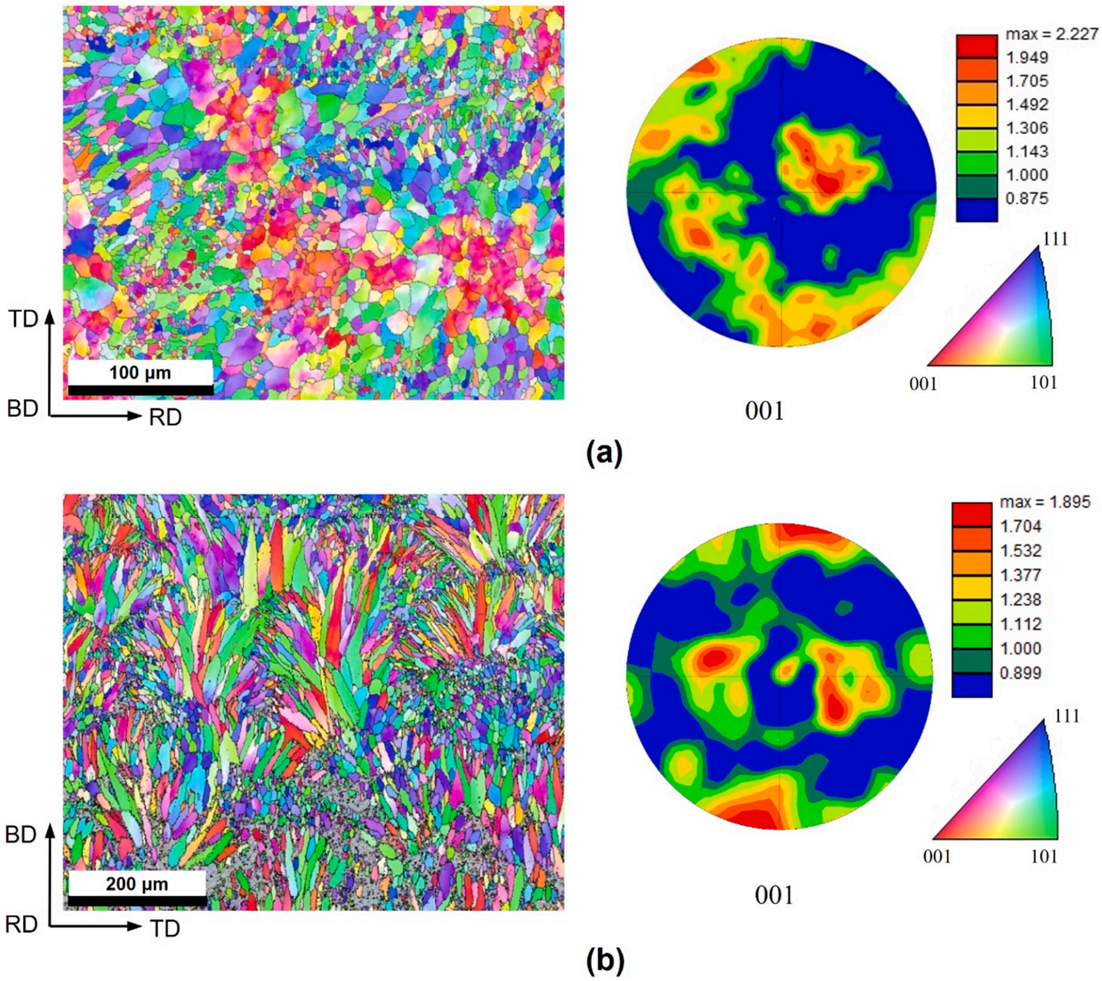

Fig. 3. The microstructure of AlSi10Mg alloy: (a) equiaxed grain morphology in the TD-RD plane; (b) columnar grain morphology in BD-TD plane. TD is the transverse direction, RD the rolling direction, and BD the building direction.

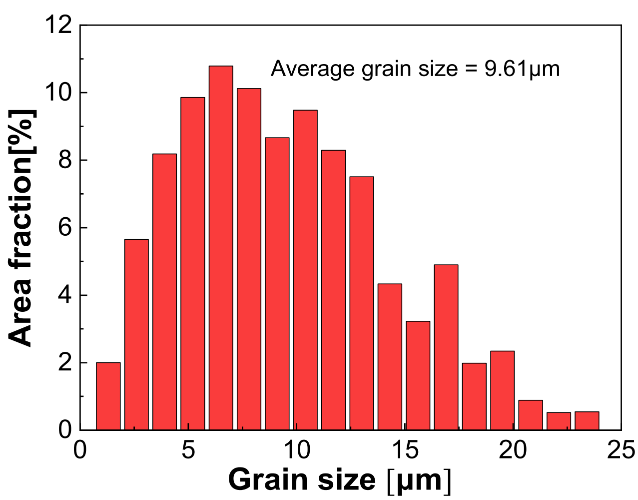

Fig. 4. Grain size distribution in the TD-RD plane.

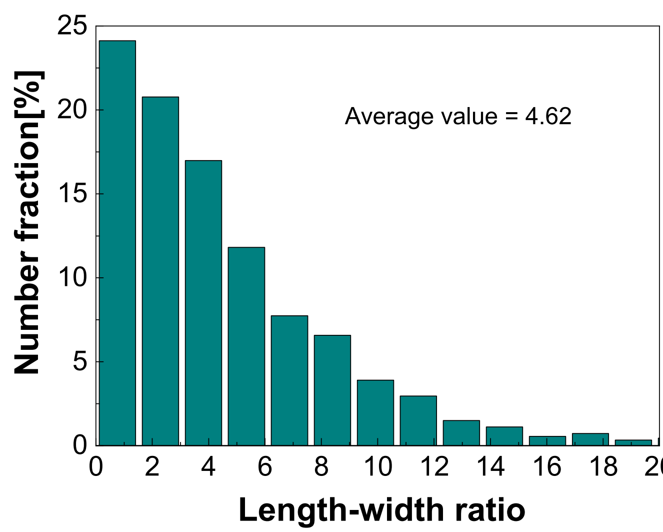

Fig. 5. The length-width ratio of the columnar grain in the BD-TD plane.

3.2. Constitutive models

Based on the Schmid law, the slipping rate $\dot{\gamma}^{\alpha}$ of the α slip system in a rate-dependent crystalline solid is determined by the corresponding resolved shear stress τ^{α} as proposed by Hutchinson [58],

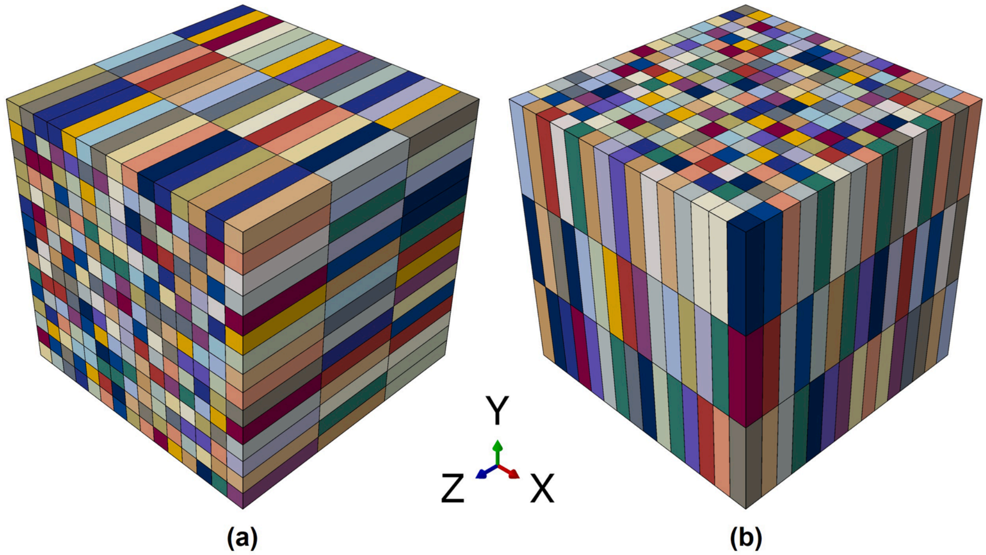

Fig. 6. The RVEs: (a) 90° sample; (b) 0° sample. The colors represent different grains within the volume.

$$\dot{\gamma}^{\alpha}=\dot{\gamma}_0\left(\frac{\tau^{\alpha}}{g^{\alpha}}\right)\left|\frac{\tau^{\alpha}}{g^{\alpha}}\right|^{n-1} \tag{10}$$

where $\dot{\gamma}_0$ is the reference shear strain rate; g^{α} is a variable which describes the current strength of the system; n is the rate sensitivity exponent.

The strain hardening is characterized by the evolution of the strengths g^{α} through the incremental relation,

$$\dot{g}^{\alpha}=\sum_{\beta=1}^{N_s} h_{\alpha\beta}|\dot{\gamma}^{\beta}| \tag{11}$$

where $h_{\alpha\beta}$ are the latent hardening moduli. The expressions of latent hardening moduli $h_{\alpha\beta}$ and self-hardening moduli $h_{\alpha\alpha}$ in the studies by Pierce et al. [59] and Asaro [60] is adopted,

$$h_{\alpha\beta} = qh(\gamma) + (1-q)h(\gamma)\delta_{\alpha\beta} \tag{12}$$

$$h_{\alpha\alpha} = h(\gamma) = h_0\mathrm{sech}^2\left|\frac{h_0\gamma}{\tau_s-\tau_0}\right| \tag{13}$$

$$\gamma=\sum_{\alpha=1}^{N_s}\int_0^t |\dot{\gamma}^{\alpha}|dt \tag{14}$$

where q is a measure for latent hardening, in most cases its value is taken as 1.0 for coplanar slip systems α and β, and 1.4 otherwise, which renders the hardening model anisotropic; h_0 is the initial hardening modulus; τ_0 is the yield shear stress; and τ_s is the saturated flow stress (or the break-through stress where large plastic flow initiates); γ is Taylor cumulative shear strain on all slip systems.

4. Finite element simulation

To evaluate the mechanical and fatigue properties of the AlSi10Mg alloy produced by SLM, the simulations, under uniaxial tension and uniaxial cyclic loading conditions, were conducted using the software ABAQUS and a user-defined material subroutine (UMAT) program based on crystal plasticity theory introduced in Section 3. The AlSi10Mg alloy has a face center cubic (FCC) structure. Hence, the dislocation glide occurs on 12 possible slip systems in the material.

4.1. Representative volume element (RVE)

In 1960s the concept of RVE was introduced as a microstructural sub/region, which is representative of the entire microstructure in an average sense. The material properties of a specimen larger than RVE can be treated equally to the average material properties of RVE. While, if a specimen is smaller than the RVE, its material properties vary according to its constituents (grains, phases, and so on) [61]. So, in order to combine micro-mechanical and coupled multi-scale approaches, an appropriate RVE of heterogeneous materials is required.

On one hand, an RVE must have enough number of grains to homogenize the variabilities arising from local microstructural features (texture, defects and chemical compositions). On the other hand, if the RVE is too big and contains too many grains, the FEM simulations can be extremely expensive. The definition of RVE size is thus extremely important for the mechanics and physics of heterogeneous materials. Numbers of approaches for the determination of RVEs have been described in the references [62-65].

In this work, we used the grain-based RVE model, in which each grain was described by many cubic elements, in order to effectively include more details about the grain shapes and sizes distribution in polycrystalline materials. From the statistical point of view, as the number of grains in the RVE increases, the response of the RVE converges to the macroscopic behaviors of the real materials.

Moussa Bouchedjra et al. [66] investigated the optimal size of RVE for polycrystal materials to predict the elastoplastic behavior using the crystal plasticity model. They validated the simulation results with corresponding experimental results on Aluminum alloy. They found that for the case (more than 200 grains), the prediction error of all quantities (tensile and cyclic tests) is less than 3%, except ratcheting strain and plastic range, which still have an error of relatively higher than 6%. For the tensile test and strain-controlled cyclic test, simulation results performed on RVE of 250 grains agree well with the experimental results. However, for the elastoplastic behavior during a stress-controlled cyclic test, the optimal RVE should have a size greater than 250 grains to assess the mechanical response of the material.

In this article, the RVE of a polycrystalline cube incorporating 675 grains were established, and random orientations were assigned to the grains within the volume (see Fig. 6), which is consistent with the EBSD results in Section 2. This RVE provides a good balance between the accuracy of the simulation results and reasonable computational efficiency. The height, width and thickness of the RVE model are all 150 μm. The short size of the columnar crystals is 10 μm according to the

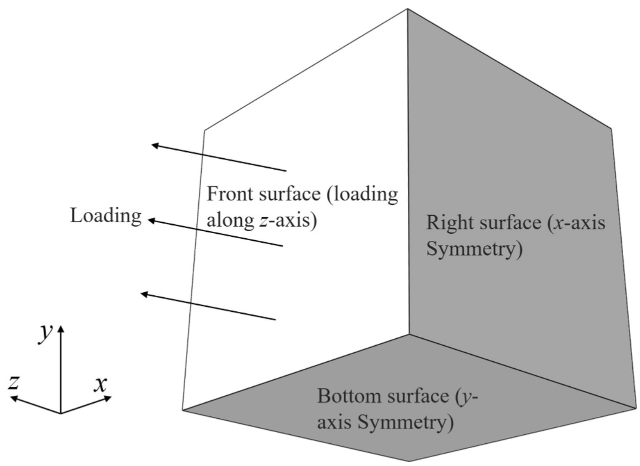

Fig. 7. Surface breakdown of the RVE to demonstrate the application of boundary conditions.

experimental results, and the long size is 50 μm (see Section 2). The RVE was then meshed using 8-node linear brick elements (C3D8I).

4.2. Boundary conditions

The boundary conditions of RVEs employed in the simulation are important to ensure their deformation response consistent with the macro-scale behavior of the material. In this study, we take 1/8 of the model and adopt the symmetric boundary conditions in the CPFE simulations as demonstrated in Fig. 7: on the right surface $U_x = UR_y = UR_z = 0$ (about x-axis symmetry); on the bottom surface $U_y = UR_x = UR_z = 0$ (about y-axis symmetry); on the back surface $U_z = UR_x = UR_y = 0$ (about z-axis symmetry); and on the front surface, the uniaxial tension or uniaxial cyclic loadings is applied along z-axis. The faces of RVEs that are not assigned a boundary condition can deform freely.

4.3. Parameter calibration

In this section, the 8 parameters (C_{11}, C_{12}, C_{44}, h_0, τ_0, τ_s, n, $\dot{\gamma}_0$) adopted in the constitutive models are calibrated with the results of uniaxial tension tests, which is shown in Table 4. For AlSi10Mg alloy, it has three independent elastic constants, C_{11}, C_{12}, C_{44}, due to the FCC symmetry. The other model parameters can be referred to the crystal plasticity theory in Section 3.

In the uniaxial tension tests, both the 90° and 0° samples were loading under a strain rate of 1×10^{-3} s^{-1}. The calibration of crystal plasticity model parameters was conducted following the try-and-error method by comparing with the tensile stress–strain curves of AlSi10Mg alloy in Fig. 8. For each of the simulation, 675 grains with different grain orientations were generated, following the same average grain size and the same set of crystal plasticity model parameters. It is seen that the tensile curve simulated by the crystal plasticity model coincided well with the experimental ones.

5. Fatigue indicator parameter (FIP) and lifetime prediction

In this work, the FIP, which should be positive and monotonically increasing with the number of loading cycles, is used to predict the fatigue lifetime of SLM-ed AlSi10Mg alloy. Based on the previous studies, including Smith-Watson-Topper's (SWT) model [67,68], works by Prithivirajan and Sangid [46], and works by Gu and co-workers [69], we assess the fatigue lifetime using different FIPs, and compared the prediction results in Section 6.

It is believed that plastic strain and local stresses are important in predicting the crack initiation events. The accumulation of plastic strain, P_{ac}, indicates the cumulative slip deformation due to the shear stresses in all slip systems. P_{ac} can be obtained by the integral of the double dot product of the plastic velocity gradient $\mathbf{L}_p$, and used in the fatigue life prediction.

$$P_{ac} = \int \sqrt{\frac{2}{3}} \mathbf{L}_P : \mathbf{L}_P dt \tag{15}$$

The first parameter FIP_1 is taken as the increment of P_{ac} in the stable loading cycles[46],

$$FIP_1 = \Delta P_{ac} = P_{ac}|_{N+1} - P_{ac}|_N \tag{16}$$

$$N_{p1} = \frac{P_{ac,c} - P_{ac,N}}{FIP_1} \tag{17}$$

Table 4
Elasticity and crystal plasticity model parameters of the SLM-ed AlSi10Mg alloy.

Samples	C_{11}[MPa]	C_{12}[MPa]	C_{44}[MPa]	$\dot{\gamma}_0$	n	h_0[MPa]	τ_s[MPa]	τ_0[MPa]
90°	100,731	60,345	30,087	0.001	90	1400	180	90
0°	100,731	60,345	30,087	0.001	90	700	188	108

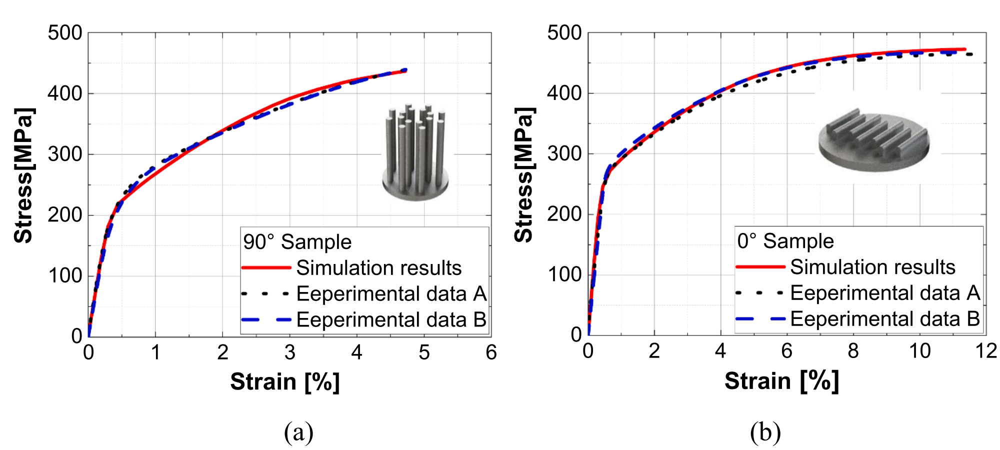

Fig. 8. Stress–strain evolution of AlSi10Mg specimens under uniaxial tensile loading: (a) 90° sample; (b) 0° sample.

Table 5
The results of ultrasonic fatigue tests for SLMed-AlSi10Mg alloy.

Number	BD	Stress ratio R	Stress amplitude σ_a (MPa)	Defect size (μm)	Experimental fatigue life
1	0° sample	−1	93	55.09	4.20E+08
2		−1	93	63.66	3.67E+08
3		−1	114	64.88	3.70E+07
4		−1	125	85.51	4.40E+07
5		0	60	71.42	6.22E+08
6		0	70	85.39	4.23E+08
7		0	80	67.29	3.32E+08
8		0.5	50	64.88	1.67E+09
9		0.5	60	50.38	1.10E+09
10		0.5	60	32.88	1.10E+09
11		0.5	65	72.26	4.74E+08
12	90°	−1	60	206.22	3.63E+08
13	sample	−1	70	105.01	1.17E+09
14		−1	75	93.69	5.81E+08
15		−1	80	184.91	1.05E+08
16		0	40	210.96	3.82E+08
17		0	40	103.3	1.11E+09
18		0	40	160	1.09E+05
19		0	50	159.28	2.15E+08

where $P_{ac,\ c}$ is the critical plastic strain when the fracture failure occurs, which can be obtained by tests; $P_{ac,\ N}$ represents the plastic strain after which the value of ΔP_{ac} becomes a constant, as is seen Fig. 11, in this study we take the subscript N as 20; N_{p1} is the corresponding fatigue lifetime.

The second model is taken as:

$$\mathrm{FIP}_2 = \mathrm{FIP}_1 \tag{18}$$

$$N_{p2} = \frac{\alpha_p}{d_{gr}(\mathrm{FIP}_2)^2} \tag{19}$$

where d_{gr} is a reference constant, which is on the order of the grain size to represent the microstructure, in this study it is 3×10^{-5}; α_p is a fitting constant, which equals 3×10^{-5} in 90° specimens, 2.5×10^{-4} in 0° specimens.

The third parameter FIP_3 is taken as the constant $\sigma_{max}\varepsilon_a$ in Smith-Watson-Topper (SWT) model. The HCF and VHCF regimes correspond to stress amplitudes below the macroscopic yield stress, thus we take the elastic part of SWT model to study the corresponding extreme fatigue life.

$$\mathrm{FIP}_3 = \sigma_{max}\varepsilon_a \tag{20}$$

$$\mathrm{FIP}_3 = \frac{\left(\sigma_f^{'}\right)^2}{E}\left(2N_{p3}\right)^{2b} \tag{21}$$

where ε_a is the elastic strain amplitude; σ'_f is the fatigue strength coefficient; E is the elastic modulus; and b is the fatigue strength exponent. In 90° specimens, $E = 62$ GPa; $\sigma'_f = 440$ MPa; $b = -0.067$. In 0° specimens, $E = 65$ GPa; $\sigma'_f = 470$ MPa; $b = -0.056$.

The calibration of the above parameters was conducted following the try-and-error method by comparing the simulation results with the experimental ones to make sure that the error is minimal. These three metrics will be used subsequently to identify the location of failure within an RVE and predict the fatigue life of each RVE.

6. Results and discussion

The frequency of ultrasonic fatigue tests is 20 kHz, thus both the 90° and 0°samples were loading under the same frequency. The results of ultrasonic fatigue tests for SLMed AlSi10Mg alloy are listed in Table 5. After the ultrasonic fatigue tests, fracture surfaces of all the broken specimens were carefully examined by SEM. The areas of the defects are equivalent to that of circles whose diameters are also listed in Table 5.

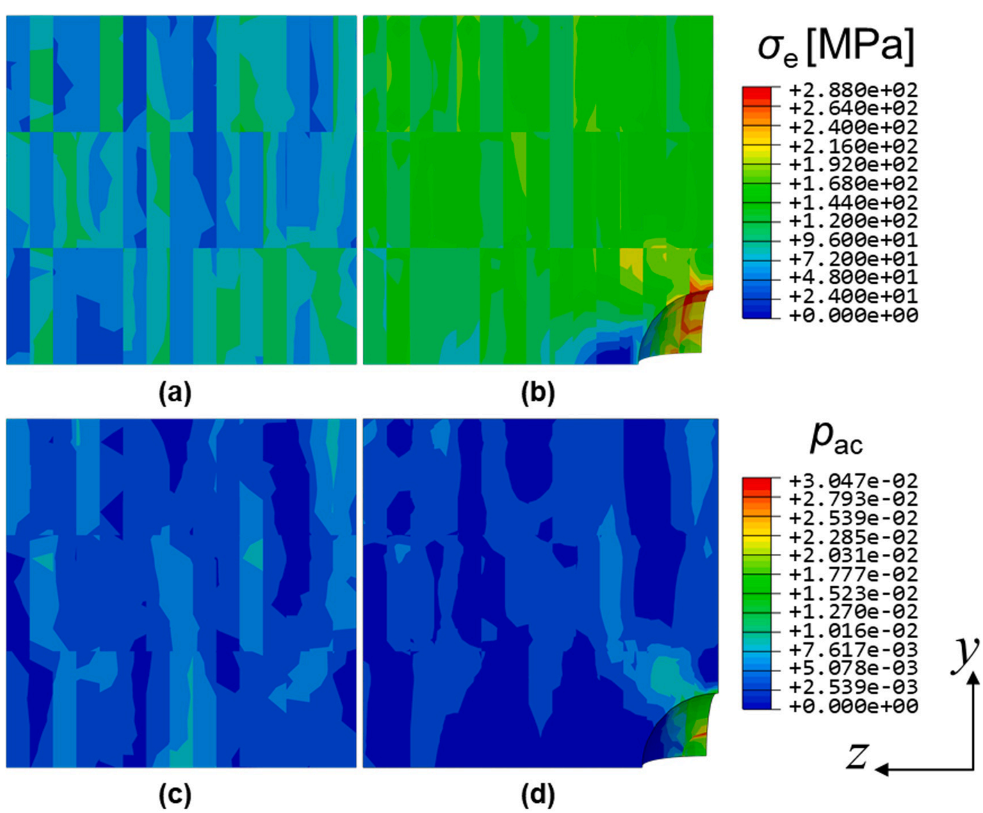

Fig. 9. The stress and plastic strain P_{ac} fields in CPFEM models of the 0°specimens under uniaxial cycle loadings, with a stress ratio of $R = 0.5$ and a stress amplitude of $\sigma_a = 50$ MPa for 50 cycles: (a, c) complete models without defects; (b, d) models with a pore of $d = 64.88$ μm.

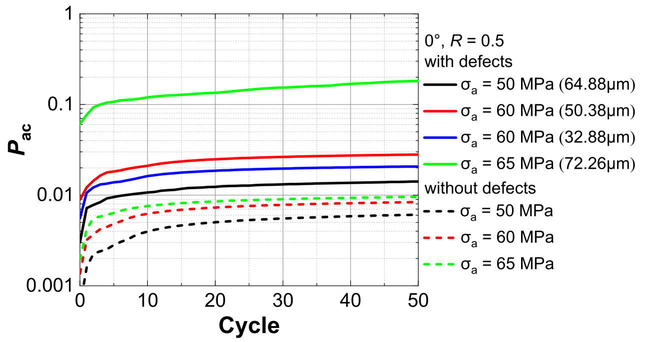

Fig. 10. The variation of P_{ac} in 0°specimens with the cycle number under different stress amplitudes σ_a. R is the stress ratio. And the defect diameters are presented in the brackets.

And in CPFE simulations, the 3D defects in RVEs are modelled as spheres whose diameters equal to that of the circles. All the cases in Table 5 have the feature that the fatigue cracks initiate from the interior of the specimens.

6.1. Stress and strain fields

The fields of Mises stress σ_e and plastic strain P_{ac} in different CPFE models for 0° specimens are shown in Fig. 9. It is clear that defects can cause stress and strain concentrations. In Fig. 9 (b) and (d), near the pore, along its vertical sides (parallel to y-axis), which is perpendicular to the loading direction (parallel to z-axis), stress and strain concentrations occur. This is consistent with the phenomenon observed in experiments that the cracks initiate from a pore on the fracture surface. And the pore can be regarded as a special case of non-sharp crack. In this case, the up and bottom regions of the pore act as the blunt crack tips, which are corresponding to the largest stress concentration regions. The stress and plastic strain fields, in different CPFE models under uniaxial cycle loadings with a stress ratio of R = -1 and 0, have a similar phenomenon with the case of $R = 0.5$ in 0° specimens. And the same phenomenon can also be seen in 90° specimens. Thus this section only offers the results in one case.

6.2. The plastic accumulated strain P_{ac}

Fig. 10 shows the variation of P_{ac} for CPFEM polycrystalline models in 0°specimens under uniaxial cyclic loadings with different stress amplitudes σ_a. It is evident that P_{ac} increases with the accumulation of loading cycles. And the larger the stress amplitudes σ_a is, the greater the plastic strain P_{ac} is. When the loading conditions are completely consistent, the larger the defect size is in the specimen, the greater the plastic strain P_{ac} is, as is shown with the red solid line and blue one.

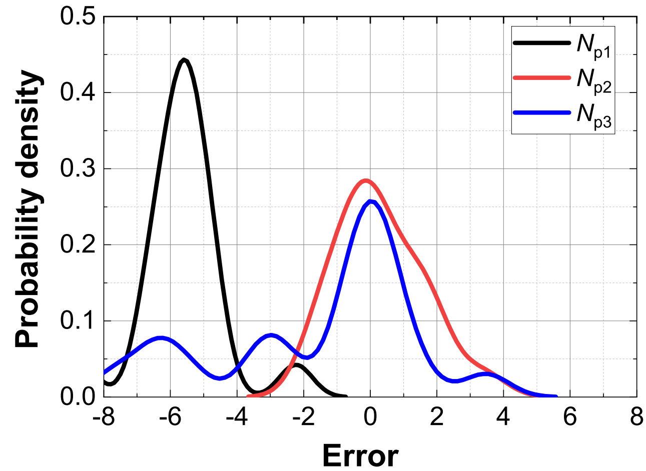

Fig. 12. Normal distribution of the error for fatigue life predicted by different models.

From Fig. 10, it can be seen that after the 20th loading cycle, the growth of P_{ac} is steady and slow, and the increment ΔP_{ac} almost remains constant. This is consistent with the study of Gillner and Münstermann [70] that the increment of local accumulated plastic shear strain kept almost constant after the initial several cycles. Then in the following study, we take the increment of plastic strain ΔP_{ac} at the 20th loading cycle, as the parameter FIP_1 (see Section 5).

The values of P_{ac}, in different CPFEM models under uniaxial cycle loadings with a stress ratio of $R = 0$ and -1, have a similar phenomenon with the case of $R = 0.5$, and the variation of P_{ac} in 90°sample is similar to that in the 0°sample, thus this section only offers the results in one case.

6.3. Fatigue life prediction

In Fig. 11, the predicted fatigue lives by different models (see Section 5, N_{p1}, N_{p2}, N_{p3}) are compared with the experimental results. It is shown that there are some fatigue life data points in models FIP_1 and FIP_3 locate without the scatter band between the two dotted lines (±2 error); while in model N_{p2}, almost all the fatigue life data points located within the scatter band. Thus, the fatigue lifetime predicted by model N_{p2} is satisfactory and more accurate than the other two models. The only datum above the scatter band in Fig. 11 (b), represents the case of $R = 0$, σ_a = 40 MPa, experimental fatigue life = 1.09×10^5, which is far less than other values and without the VHCF regime. This could because that there are sharp defects within the specimen.

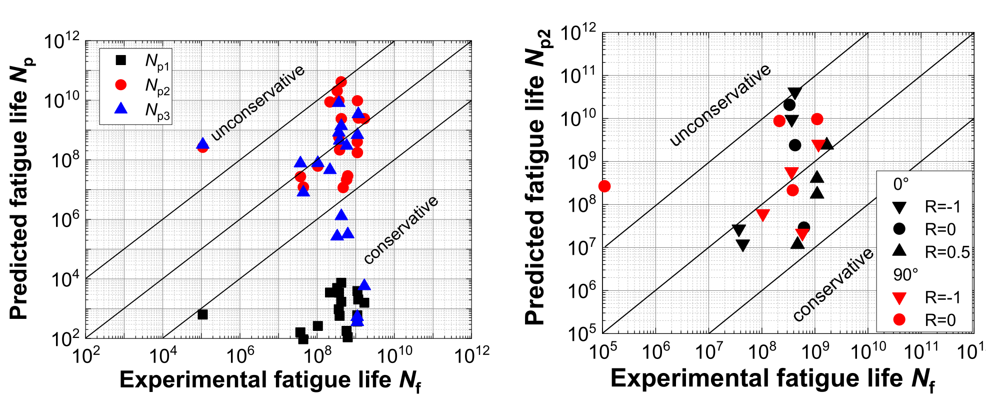

(a)   (b)

Fig. 11. Comparison of the predicted fatigue lives by different models versus the experimental ones.

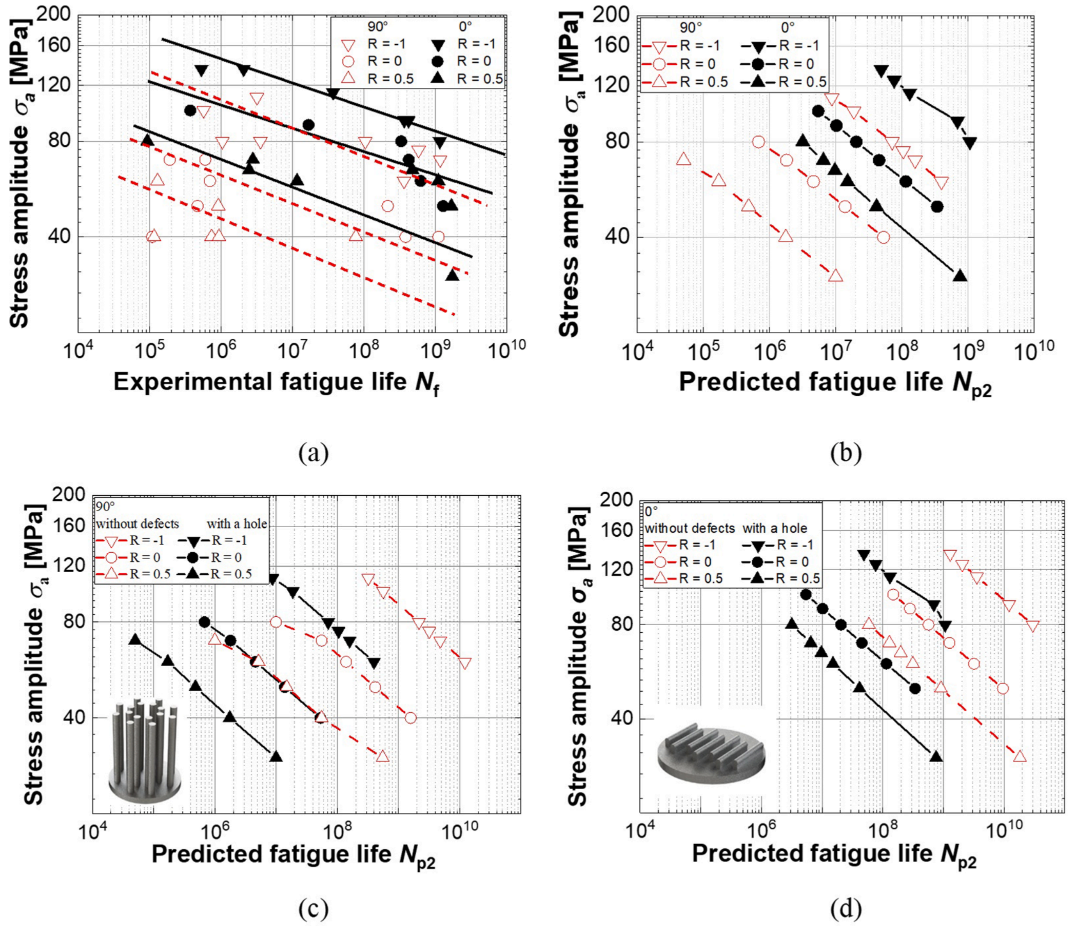

Fig. 13. S-N curves by different models for AlSi10Mg specimens: (a) experimental data; (b) predicted values by model N_{p2} with a hole in the specimen; (c) comparison between the results predicted by model N_{p2} in 90°specimens with a hole and without defects; (d) comparison between the results predicted by model N_{p2} in 0°specimens with a hole and without defects.

In Fig. 12, the normal distribution of the error for fatigue life predicted by different models is presented. The peak values of these three curves represent the probability of their average error. So, the closer the average error is to 0, the more accurate the fatigue life prediction is. From Fig. 12, it is obvious that models N_{p2} and N_{p3} are better than model N_{p1}. In addition, the error distributions of model N_{p1} and N_{p3} have a larger range, indicating that the variance of the predicted fatigue life is greater. So, the prediction values of model N_{p1} and N_{p3} are instability. In contrast, the fatigue life prediction of model N_{p2} is more reliable.

In summary, the prediction of fatigue life by model N_{p2} is in good agreement with the test results. Therefore, model N_{p2} is recommended for fatigue life prediction of SLM-ed AlSi10Mg in VHCF regime.

$$\text{error} = log_{10}(N_p) - log_{10}(N_f) \tag{22}$$

where N_p is the predicted fatigue life, and N_f is the experimental fatigue life under the same loading condition.

Fig. 13 shows the S-N curves predicted by different models for SLM-ed AlSi10Mg specimens. In Fig. 13 (a), the experimental results indicate that the stress ratio plays an important role in HCF and VHCF properties. With the increase of the stress ratio, the fatigue strength decreases. In addition, the build orientation has an important effect on the fatigue property. The fatigue strength of 90° specimens is obviously lower than that of 0° specimens. In Fig. 13 (b), the predicted results by model N_{p2} show similar phenomena with Fig. 13 (a). Fig. 13 (c) and (d) demonstrate that defects can obviously reduce the HCF and VHCF fatigue performance of the specimen. The fatigue life of the sample with a hole is about 2 orders lower than that of the sample with no defects. The effect of defects on the 90° built specimens is a little larger than that of 0° built specimens. There are two reasons for this. One reason is that both in 90° and 0° built specimens the stresses is applied along z-axis. However, the long axis directions of columnar crystals in 90° and 0° specimens are along z-axis and y-axis, respectively, due to the different building directions. The other reason is that the defect size of 90° built specimens is larger than that of 0° built specimens.

7. Conclusions

In the present study, the crystal plasticity finite element model is used to study the cyclic plasticity behavior and high-cycle fatigue and very-high-cycle fatigue properties of AlSi10Mg alloy fabricated by the selective laser melting process. The following conclusions have been obtained:

(1) The HCF and VHCF fatigue life of the alloy predicted by model N_{p2} is in good agreement with the experimental results and the model N_{p2} is relatively reliable.
(2) The build orientation has a great effect on the fatigue performance of SLM-ed AlSi10Mg. 0° specimens have a better performance than 90° specimens.
(3) Defects significantly reduce the HCF and VHCF fatigue performance of the specimens. The fatigue lifetime of the sample with a hole is about 2 orders lower than that of the sample without defect. The effect of defects on the 90° built specimens is slightly larger than that of 0° built specimens.

(4) The stress ratio plays an important role in HCF and VHCF properties. With the increase of the stress ratio, the fatigue strength decreases.

Declaration of Competing Interest

The authors declare that they have no known competing financial interests or personal relationships that could have appeared to influence the work reported in this paper.

Acknowledgements

This work was funded by the NSFC Basic Science Center Program for "Multiscale Problems in Nonlinear Mechanics" (No.11988102), the National Natural Science Foundation of China (No. 11872364, 11932020, 12072345, 12002185), National Science and Technology Major Project (J2019-VI-0012-0126) and CAS Pioneer Hundred Talents Program.

References

[1] Hirsch J. Aluminium alloys for automotive application. Mater Sci Forum 1997;242:33–50.
[2] Dursun T, Soutis C. Recent developments in advanced aircraft aluminium alloys. Mater Design 2014;56:862–71.
[3] Sweet GA, Hexemer RL, Donaldson IW, Taylor A, Bishop DP. Powder metallurgical processing of a 2xxx series aluminum powder metallurgy metal alloy reinforced with AlN particulate additions. Mater Sci Eng, A 2019;755:10–7.
[4] Ponnusamy P, Rahman Rashid RA, Masood SH, Ruan D, Palanisamy S. Mechanical properties of SLM-printed aluminium alloys: A review. Materials 2020;13(19):4301. https://doi.org/10.3390/ma13194301.
[5] Aboulkhair NT, Simonelli M, Parry L, Ashcroft I, Tuck C, Hague R. 3D printing of aluminium alloys: Additive manufacturing of aluminium alloys using selective laser melting. Prog Mater Sci 2019;106:100578. https://doi.org/10.1016/j.pmatsci.2019.100578.
[6] Frazier WE. Metal additive manufacturing: A review. J Mater Eng Perform 2014;23(6):1917–28.
[7] Yadollahi A, Shamsaei N. Additive manufacturing of fatigue resistant materials: Challenges and opportunities. Int J Fatigue 2017;98:14–31.
[8] Aboulkhair NT, Maskery I, Tuck C, Ashcroft I, Everitt NM. Improving the fatigue behaviour of a selectively laser melted aluminium alloy: Influence of heat treatment and surface quality. Mater Design 2016;104:174–82.
[9] Suryawanshi J, Prashanth KG, Scudino S, Eckert J, Prakash Om, Ramamurty U. Simultaneous enhancements of strength and toughness in an Al-12Si alloy synthesized using selective laser melting. Acta Mater 2016;115:285–94.
[10] Mower TM, Long MJ. Mechanical behavior of additive manufactured, powder-bed laser-fused materials. Mater Sci Eng, A 2016;651:198–213.
[11] Xu ZW, Wang Q, Wang XS, Tan CH, Guo MH, Gao PB. High cycle fatigue performance of AlSi10mg alloy produced by selective laser melting. Mech Mater 2020;148:103499. https://doi.org/10.1016/j.mechmat.2020.103499.
[12] Beevers E, Brandão AD, Gumpinger J, Gschweitl M, Seyfert C, Hofbauer P, et al. Fatigue properties and material characteristics of additively manufactured AlSi10Mg – Effect of the contour parameter on the microstructure, density, residual stress, roughness and mechanical properties. Int J Fatigue 2018;117:148–62.
[13] Tang M, Pistorius PC. Fatigue life prediction for AlSi10Mg components produced by selective laser melting. Int J Fatigue 2019;125:479–90.
[14] Read N, Wang W, Essa K, Attallah MM. Selective laser melting of AlSi10Mg alloy: Process optimisation and mechanical properties development. Mater Design 2015;65:417–24.
[15] Brandl E, Heckenberger U, Holzinger V, Buchbinder D. Additive manufactured AlSi10Mg samples using Selective Laser Melting (SLM): Microstructure, high cycle fatigue, and fracture behavior. Mater Design 2012;34:159–69.
[16] Serrano-Munoz I, Buffiere JY, Mokso R, Verdu C, Nadot Y. Location, location & size: defects close to surfaces dominate fatigue crack initiation. Sci Rep 2017;7:45239.
[17] Hu YN, Wu SC, Withers PJ, Zhang J, Bao HYX, Fu YN, et al. The effect of manufacturing defects on the fatigue life of selective laser melted Ti-6Al-4V structures. Mater Design 2020;192:108708. https://doi.org/10.1016/j.matdes.2020.108708.
[18] Romano S, Abel A, Gumpinger J, Brandão AD, Beretta S. Quality control of AlSi10Mg produced by SLM: Metallography versus CT scans for critical defect size assessment. Addit Manuf 2019;28:394–405.
[19] Wu Z, Wu S, Bao J, Qian W, Karabal S, Sun W, et al. The effect of defect population on the anisotropic fatigue resistance of AlSi10Mg alloy fabricated by laser powder bed fusion. Int J Fatigue 2021;151:106317. https://doi.org/10.1016/j.ijfatigue.2021.106317.
[20] Siddique S, Imran M, Wycisk E, Emmelmann C, Walther F. Fatigue assessment of laser additive manufactured AlSi12 eutectic alloy in the very high cycle fatigue (VHCF) range up to 1E9 cycles. Mater Today: Proc 2016;3(9):2853–60.
[21] Ghouse S, Babu S, Nai K, Hooper PA, Jeffers JRT. The influence of laser parameters, scanning strategies and material on the fatigue strength of a stochastic porous structure. Addit Manuf 2018;22:290–301.
[22] Greitemeier D, Palm F, Syassen F, Melz T. Fatigue performance of additive manufactured TiAl6V4 using electron and laser beam melting. Int J Fatigue 2017;94:211–7.
[23] Ren S, Chen Y, Liu T, Qu X. Effect of build orientation on mechanical properties and microstructure of Ti-6Al-4V manufactured by selective laser melting. Metall Mater Trans A 2019;50(9):4388–409.
[24] Yang KV, Rometsch P, Davies CHJ, Huang A, Wu X. Effect of heat treatment on the microstructure and anisotropy in mechanical properties of A357 alloy produced by selective laser melting. Mater Design 2018;154:275–90.
[25] Xu ZW, Liu A, Wang XS. The influence of building direction on the fatigue crack propagation behavior of Ti6Al4V alloy produced by selective laser melting. Mater Sci Eng, A 2019;767:138409. https://doi.org/10.1016/j.msea.2019.138409.
[26] Oliveira JP, Santos TG, Miranda RM. Revisiting fundamental welding concepts to improve additive manufacturing: from theory to practice. Prog Mater Sci 2020;107:100590. https://doi.org/10.1016/j.pmatsci.2019.100590.
[27] Basquin OH. The exponential law of endurance tests. Proc Am Soc Test Mater 1910;10:625–30.
[28] Coffin Jr LF. A study of the effects of cyclic thermal stresses on a ductile metal. Trans Am Soc Mech Eng 1954;76:931–50.
[29] Manson SS. Behavior of materials under conditions of thermal stress. Cleveland, OH: National Advisory Committee for Aeronautics; 1953.
[30] Morrow JoDean. In: Internal Friction, Damping, and Cyclic Plasticity. 100 Barr Harbor Drive, PO Box C700, West Conshohocken, PA 19428-2959: ASTM International; 1965. 45–45-43. https://doi.org/10.1520/STP43764S.
[31] Park J, Nelson D. Evaluation of an energy-based approach and a critical plane approach for predicting constant amplitude multiaxial fatigue life. Int J Fatigue 2000;22:23–39.
[32] Jahed H, Varvanifarahani A, Noban M, Khalaji I. An energy-based fatigue life assessment model for various metallic materials under proportional and non-proportional loading conditions. Int J Fatigue 2007;29(4):647–55.
[33] Bandyopadhyay R, Prithivirajan V, Peralta AD, Sangid MD. Microstructure-sensitive critical plastic strain energy density criterion for fatigue life prediction across various loading regimes. Proc Math Phys Eng Sci 2020;476(2236):20190766. https://doi.org/10.1098/rspa.2019.0766.
[34] Hong Y, Sun C. The nature and the mechanism of crack initiation and early growth for very-high-cycle fatigue of metallic materials – An overview. Theor Appl Fract Mech 2017;92:331–50.
[35] Wang QY, Berard JY, Rathery S, Bathias C. High-cycle fatigue crack initiation and propagation behaviour of high-strength spring steel wires. Fatigue Fract Eng M 1999;22:673–7.
[36] Hong Y, Lei Z, Sun C, Zhao A. Propensities of crack interior initiation and early growth for very-high-cycle fatigue of high strength steels. Int J Fatigue 2014;58:144–51.
[37] Takai K, Seki J, Homma Y. Observation of trapping sites of hydrogen and deuterium in high-strength steels by using secondary ion mass spectrometry. Mater T JIM 1995;36(9):1134–9.
[38] Shiozawa K, Lu L, Ishihara S. S-N curve characteristics and subsurface crack initiation behaviour in ultra-long life fatigue of a high carbon– chromium bearing steel. Fatigue Fract Eng M 2001;24(12):781–90.
[39] Murakami Y, Nomoto T, Ueda T, Murakami Y. On the mechanism of fatigue failure in the superlong life regime (N > 107 cycles), Part II: a fractographic investigation. Fatigue Fract Eng M 2000;23:903–10.
[40] Zhao A, Xie J, Sun C, Lei Z, Hong Y. Effects of strength level and loading frequency on very-high-cycle fatigue behavior for a bearing steel. Int J Fatigue 2012;38:46–56.
[41] Murakami Y, Kodama S, Konuma S. Quantitative evaluation of effects of non-metallic inclusions on fatigue strength of high strength steels. I: Basic fatigue mechanism and evaluation of correlation between the fatigue fracture stress and the size and location of non-metallic inclusions. Int J Fatigue 1989;11(5):291–8.
[42] Hong Y, Liu X, Lei Z, Sun C. The formation mechanism of characteristic region at crack initiation for very-high-cycle fatigue of high-strength steels. Int J Fatigue 2016;89:108–18.
[43] McDowell DL. Simulation-based strategies for microstructure-sensitive fatigue modeling. Mater Sci Eng, A 2007;468-470:4–14.
[44] Sangid MD, Maier HJ, Sehitoglu H. An energy-based microstructure model to account for fatigue scatter in polycrystals. J Mech Phys Solids 2011;59(3):595–609.
[45] Agius D, Mamun AA, Simpson CA, Truman C, Wang Y, Mostafavi M, et al. Microstructure-informed, predictive crystal plasticity finite element model of fatigue-dwells. Comp Mater Sci 2020;183:109823. https://doi.org/10.1016/j.commatsci.2020.109823.
[46] Prithivirajan V, Sangid MD. Examining metrics for fatigue life predictions of additively manufactured IN718 via crystal plasticity modeling including the role of simulation volume and microstructural constraints. Mater Sci Eng, A 2020;783:139312. https://doi.org/10.1016/j.msea.2020.139312.
[47] Roters F, Diehl M, Shanthraj P, Eisenlohr P, Reuber C, Wong SL, et al. DAMASK – The Düsseldorf Advanced Material Simulation Kit for modeling multi-physics crystal plasticity, thermal, and damage phenomena from the single crystal up to the component scale. Comp Mater Sci 2019;158:420–78.
[48] Roters F, Eisenlohr P, Hantcherli L, Tjahjanto DD, Bieler TR, Raabe D. Overview of constitutive laws, kinematics, homogenization and multiscale methods in crystal plasticity finite-element modeling: Theory, experiments, applications. Acta Mater 2010;58(4):1152–211.

[49] Fatemi A, Socie DF. A critical plane approach to multiaxial fatigue damage including out-of-phase loading. Fatigue Fract Eng M 1988;11(3):149–65.
[50] Castelluccio GM, McDowell DL. Microstructure and mesh sensitivities of mesoscale surrogate driving force measures for transgranular fatigue cracks in polycrystals. Mater Sci Eng, A 2015;639:626–39.
[51] Castelluccio GM, McDowell DL. Mesoscale modeling of microstructurally small fatigue cracks in metallic polycrystals. Mater Sci Eng, A 2014;598:34–55.
[52] Przybyla CP, Musinski WD, Castelluccio GM, McDowell DL. Microstructure-sensitive HCF and VHCF simulations. Int J Fatigue 2013;57:9–27.
[53] Castelluccio GM, McDowell DL. A mesoscale approach for growth of 3D microstructurally small fatigue cracks in polycrystals. Int J Damage Mech 2013;23: 791–818.
[54] McDowell DL, Dunne FPE. Microstructure-sensitive computational modeling of fatigue crack formation. Int J Fatigue 2010;32(9):1521–42.
[55] Jian ZM, Qian GA, Paolino DS, Tridello A, Berto F, Hong YS. Crack initiation behavior and fatigue performance up to very-high-cycle regime of AlSi10Mg fabricated by selective laser melting with two powder sizes. Int J Fatigue 2021;143: 106013. https://doi.org/10.1016/j.ijfatigue.2020.106013.
[56] Rice JR. Inelastic constitutive relations for solids: An internal-variable theory and its application to metal plasticity. J Mech Phys Solids 1971;19(6):433–55.
[57] Hill R, Rice JR. Constitutive analysis of elastic-plastic crystals at arbitrary strain. J Mech Phys Solids 1972;20(6):401–13.
[58] Hutchinson JW. Bounds and self-consistent estimates for creep of polycrystalline materials. P Roy Soc A-Math Phy 1976;348:101–27.
[59] Peirce D, Asaro RJ, Needleman A. An analysis of nonuniform and localized deformation in ductile single crystals. Acta Metall 1982;30(6):1087–119.
[60] Asaro RJ. Crystal plasticity. J Appl Mech 1983;50:922.
[61] Simonovski I, Cizelj L. Representative Volume Element Size of a Polycrystalline Aggregate with Embedded Short Crack. International conference: Nuclear energy for new Europe. 2007.
[62] El Moumen A, Kanit T, Imad A. Numerical evaluation of the representative volume element for random composites. Eur J Mech A-Solid 2021;86:104181. https://doi.org/10.1016/j.euromechsol.2020.104181.
[63] Lim H, Battaile CC, Bishop JE, Foulk JW. Investigating mesh sensitivity and polycrystalline RVEs in crystal plasticity finite element simulations. Int J Plasticity 2019;121:101–15.
[64] Mirkhalaf SM, Andrade Pires FM, Simoes R. Determination of the size of the Representative Volume Element (RVE) for the simulation of heterogeneous polymers at finite strains. Finite Elem Anal Des 2016;119:30–44.
[65] Pelissou C, Baccou J, Monerie Y, Perales F. Determination of the size of the representative volume element for random quasi-brittle composites. Int J Solids Struct 2009;46(14-15):2842–55.
[66] Bouchedjra M, Kanit T, Boulemia C, Amrouche A, Belouchrani MEA. Determination of the RVE size for polycrystal metals to predict monotonic and cyclic elastoplastic behavior: Statistical and numerical approach with new criteria. Eur J Mech A-Solid 2018;72:1–15.
[67] Li J, Liu J, Sun Q, Zhang ZP, Qiao YJ. A modification of Smith–Watson–Topper damage parameter for fatigue life prediction under non-proportional loading. Fatigue Fract Eng M 2011;35:301–16.
[68] Ince A, Glinka G. A modification of Morrow and Smith–Watson–Topper mean stress correction models. Fatigue Fract Eng M 2011;34:854–67.
[69] Gu C, Lian J, Bao Y, Xie Q, Münstermann S. Microstructure-based fatigue modelling with residual stresses: Prediction of the fatigue life for various inclusion sizes. Int J Fatigue 2019;129:105158. https://doi.org/10.1016/j.ijfatigue.2019.06.018.
[70] Gillner K, Münstermann S. Numerically predicted high cycle fatigue properties through representative volume elements of the microstructure. Int J Fatigue 2017; 105:219–34.